Materials Advances

ROYAL SOCIETY OF CHEMISTRY

PAPER

View Article Online
View Journal | View Issue

Cite this: *Mater. Adv.*, 2026, 7, 5116

Barocaloric and magnetocaloric effects in the A-site layer-ordered double perovskite $YBaCo_2O_{5.5}$

Mayuri Ito, Masato Goto,* Kevin Iputera and Yuichi Shimakawa*

Searching for novel caloric materials is essential for realizing environmentally friendly, energy-efficient refrigeration systems. The A-site layer-ordered double perovskite oxide $YBaCo_2O_{5.5}$, which had a degree of freedom for the Co^{3+}-spin state, was found to exhibit caloric effects by applying multiple external fields regarding three observed phase transitions. Large latent heat of 8.8 J g^{-1} is observed near the first-order metal–insulator–transition temperature (close to room temperature), where a negative-thermal-expansion-like volume change and a change in the Co^{3+}-spin state are accompanied. Significantly, the corresponding entropy change of 29.8 J K^{-1} kg^{-1} can be utilized through an inverse barocaloric effect. The ferrimagnetic and antiferromagnetic transitions below the metal–insulator transition temperature can be controlled by applying magnetic fields, inducing normal and inverse magnetocaloric effects, respectively. In addition, when a high magnetic field above 10 kOe is applied, the second-order ferrimagnetic transition merges with the first-order metal–insulator transition as a single first-order transition, potentially enhancing the barocaloric effect. These thermal properties provide valuable insight into the development of efficient refrigeration by means of transition-metal oxides.

Received 18th February 2026,
Accepted 8th April 2026

DOI: 10.1039/d6ma00234j

rsc.li/materials-advances

Introduction

In recent years, thermal control has become one of the most critical issues, driven by global warming, increased heat generation from precision equipment in the advanced information society, and the freezing and storage of large amounts of food for long periods. Caloric effects of solids are attracting attention as an alternative to the current gas-compression method. The use of solid-caloric-effect materials allows for environmentally friendly, energy-efficient, and compact cooling systems.[1] In the caloric effects, entropy changes in response to external fields lead to practical thermal conversions, and magnetocaloric, electrocaloric, and barocaloric effects are typical responses to magnetic, electric, and pressure fields, respectively.[2–8]

Significant entropy changes are often induced near the phase-transition temperature, leading to substantial caloric effects.[4,9,10] In particular, materials that exhibit first-order transitions have latent heat, so more significant caloric effects can be expected.[10–12] Several benchmark materials have demonstrated giant thermal responses near their first-order phase transitions. For example, $Gd_5(Si, Ge)_4$ and $La(Fe, Si)_{13}$-based alloys are well-known for their giant magnetocaloric effects, exhibiting magnetic entropy changes ΔS exceeding 15.0 J K^{-1} kg^{-1} under moderate magnetic fields.[10,13] Transition-metal oxides, which correspond to chemically stable inorganic solid materials, are good candidates to show large latent heat due to their strong electron-lattice coupling.[14,15] Indeed, we recently reported large latent heat and the corresponding colossal barocaloric effect (ΔS = 65.1 J K^{-1} kg^{-1} under 5.1 kbar) in the A-site-quadrupole perovskite $NdCu_3Fe_4O_{12}$.[16] In $NdCu_3Fe_4O_{12}$, the instability of usually high valence $Fe^{3.75+}$ induces first-order inter-site charge transfer between Cu and Fe ions near room temperature, which accompanies a metal–insulator transition, a negative-thermal-expansion-like cell–volume change, and a paramagnetic-antiferromagnetic transition simultaneously.[16] While $NdCu_3Fe_4O_{12}$ shows the barocaloric effect, the latent heat cannot be utilized through a magnetocaloric effect because the antiferromagnetic transition cannot be controlled by applying a magnetic field.

After the discovery of $NdCu_3Fe_4O_{12}$, we expanded the search range for the substances to a perovskite-related Co^{3+} oxide $YBaCo_2O_{5.5}$, which has a degree of freedom for the Co^{3+} spin state. $YBaCo_2O_{5.5}$ was reported to show exotic successive phase transitions, which include a Co^{3+}-spin-state-change induced first-order metal–insulator transition with a cell-volume change near room temperature and two magnetic transitions (from paramagnetic to antiferromagnetic through ferrimagnetic) below the first-order transition temperature.[17,18] In this paper, we report thermal properties regarding the successive phase transitions in the A-site-layer-ordered double perovskite $YBaCo_2O_{5.5}$. We discovered caloric effects by applying multiple external fields, which means both barocaloric and magnetocaloric effects. The metal–insulator transition accompanies a

Institute for Chemical Research, Kyoto University, Uji, Kyoto 611-0011, Japan.
E-mail: goto.masato.8s@kyoto-u.ac.jp

large latent heat, which can be utilized *via* a barocaloric effect. In addition, $YBaCo_2O_{5.5}$ shows both normal and inverse magnetocaloric effects in the vicinity of the two magnetic phase transitions.

Experimental

Approximately 1.0 g of pellet-shaped polycrystalline sample of $YBaCo_2O_{5.5}$ was prepared by a conventional solid-state reaction similar to that reported by Akahoshi *et al.*, using Y_2O_3, $BaCO_3$, and Co_3O_4.[17] A portion of the obtained pellet sample was ground into a fine powder for synchrotron X-ray diffraction (SXRD) measurements using the BL02B2 beamline at SPring-8 (λ = 0.4958 and 0.4999 Å). The powder sample was packed into a silica capillary rotated during the measurement. The data obtained were analysed with the Rietveld method using the RIETAN-FP program.[19,20] The corresponding crystal structure models were drawn using the VESTA software.[21]

For measurements other than SXRD, pellet samples cut into appropriate sizes were used. Differential scanning calorimetry was carried out at heating and cooling rates of 10 °C min^{-1}. using NETZSCH DSC3500. The heat flow curves were obtained by subtracting the base change. The latent heat Q and the entropy change S associated with the transition were calculated as $Q = \int_{T_a}^{T_b}(d\dot{Q}/\dot{T})dT$ and $S = \int_{T_a}^{T_b}\{(-d\dot{Q}/\dot{T})/T\}dT$, where $d\dot{Q}$ is the heat flow and $\dot{T}$ is the cooling or heating rate.

Differential thermal analysis (DTA) measurements were performed using a pressure cylinder made of Cu–Be. The details of the equipment and the setup are described in the ref. 4. A T-type thermocouple was adhered with varnish to each sample and the CuO reference pellet. The DTA cell with Daphne7373 pressure medium was inserted in the pressure cylinder. A hydraulic cylinder applied hydrostatic pressure *via* a piston. The sample temperature was controlled using a mantle heater. The heat flow (divided by heating rate) curves were obtained with the DTA signal δT as $dq/dT = -A\delta T/\dot{T}$. Because the proportional constant A scarcely changed during measurements with the same setup conditions under pressure, the A value was determined from the heat flow $\dot{Q}$ measured by DSC under an ambient condition. The entropy was evaluated as the following equation.

$$S(T,P) = \int_{T_a}^{T_b}\{(-A\delta T(P)/\dot{T})/T\}dT \qquad (1)$$

The isothermal entropy change at each pressure wasalculated as $\Delta S_P = S(T, P) - S(T, 0)$.

DC magnetization measurements were performed using a superconducting quantum interference device (SQUID; Quantum Design MPMS-XL) over the temperature range 200–320 K. All the magnetization measurements were conducted under field cooling conditions. The maximum (or the minimum) value of dM/dT is defined as the magnetic transition temperature T_N (T_C).

Electrical resistivity was measured using the standard four-probe method with a Physical Property Measurement System (PPMS). The sample was a rectangular sintered pellet with dimensions of 2.8 mm in width, 3.0 mm in length, and 0.6 mm in thickness. Silver wires were attached to the pellet using silver paste to ensure electrical contact.

Results and discussion

Single-phase sample of A-site layer-ordered double perovskite $YBaCo_2O_{5.5}$ was successfully synthesized. As shown in Fig. S1(a), all the observed SXRD peaks at 300 K can be well fitted with an orthorhombic $2a_p \times 2a_p \times 2a_p$ cell, adopting the space group *Pmma* (a_p denotes the lattice constant of the simple perovskite). Notably, the precise structural refinement confirms nearly perfect ordering between Y/Ba at the A site. The obtained compound was confirmed to exhibit successive phase transitions as follows. In the electrical resistivity data, an abrupt increase is observed at T_{MI} = 295 K (Fig. 1), indicating a metal–insulator (MI) transition. Associated with the MI transition, a discontinuous jump in the lattice constants and a discontinuous volume change with negative thermal expansion (ΔV = −0.12%) are induced at T_{MI}, confirming a first-order structural transition. The crystal structure changes to the *P*2/*c* monoclinic $2a_p \times 2a_p \times 2a_p$ cell at T_{MI} [Fig. S1(b), Fig. S2 and Table S1], which is consistent with the report by Pantoja.[22] In the temperature dependence of the magnetization, following a slight anomaly at T_{MI} = 295 K, a paramagnetic-ferrimagnetic (PM-FiM) transition at T_C = 288 K and a ferrimagnetic-antiferromagnetic (FiM-AFM) transition at T_N = 266 K are observed. While no structural change is observed at T_C and T_N, a slight increase in the electric resistivity is also induced at T_N. Further decreasing the temperature, the crystal structure returns to the *Pmma* orthorhombic $2a_p \times 2a_p \times 2a_p$ cell at T_s = 230 K (Fig. S2). A positive thermal-expansion-like discontinuous volume change is also observed at T_s = 230 K, indicating a first-order structural

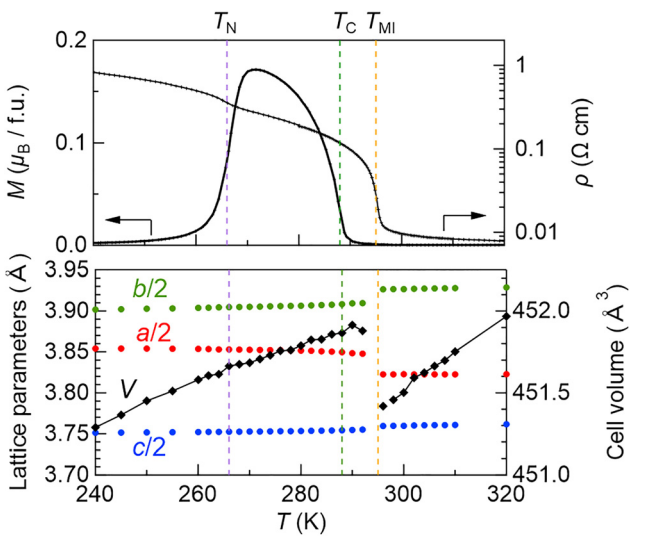

Fig. 1 Temperature dependence of the magnetization, the electrical resistivity (top), lattice constants, and cell volume (bottom) of $YBaCo_2O_{5.5}$. Vertical dashed lines indicate three phase-transition temperatures.

transition. These four phase-transition temperatures are in good agreement with those reported previously, confirming the target composition $YBaCo_2O_{5.5}$ with the appropriate oxygen content.[17,18,22]

Among the four phase transitions, the first-order transition at T_{MI} = 295 K was found to have a large latent heat. Fig. 2 shows a DSC curve and the corresponding entropy change. The DSC data includes a prominent peak at approximately 295 K and a tiny peak at approximately 264 K. The former peak corresponds to the first-order transition at T_{MI}, while the latter one corresponds to the magnetic transition at T_N. On the other hand, no significant peak is observed at T_s = 230 K, despite the presence of the first-order phase transition accompanied by the discontinuous volume change. Notably, near the phase transition at T_{MI}, the large latent heat of 8.8 J g^{-1} is observed. The corresponding entropy change is 29.8 J K^{-1} kg^{-1}, which is obviously smaller than that of $NdCu_3Fe_4O_{12}$ (84.2 J K^{-1} kg^{-1}), but still significant in oxide materials.[14,16,23]

The large latent heat can be utilized through a barocaloric effect (BCE) by applying hydrostatic pressure. Fig. 3(a) shows the heat flow $-dq/dT$ obtained by differential thermal analysis (DTA) measurements at various pressures. As the applied pressure increases, the DTA peak corresponding to the structural transition at T_{MI} shifts to lower temperatures, suggesting an inverse BCE. The decrease in T_{MI} is related to the stabilization of the high-temperature (metallic) phase, which has a smaller cell volume. The pressure dependence of T_{MI} is summarized in Fig. 3(b). Applying pressure results in a linear decrease in T_{MI}, with a pressure coefficient of dT_{MI}/dP = −0.91 K $kbar^{-1}$. The experimental coefficient can be compared with that obtained from the Clausius–Clapeyron equation

$$dT/dP = \Delta V_{tr}/\Delta S_{tr}, \quad (2)$$

where ΔS_{tr} and ΔV_{tr} are the entropy and volume changes at the first-order phase transition, respectively. Using experimentally obtained $\Delta V_{tr} = 18.98 \times 10^{-8}$ m^3 kg^{-1} and ΔS_{tr} = 29.8 J K^{-1} kg^{-1}, dT/dP was calculated to be 0.64 K $kbar^{-1}$, which is roughly consistent with the experimental value. It is worth noting that the DTA peak under P = 6 kbar hardly overlaps with that at ambient pressure, allowing the large latent to be utilized almost entirely as the BCE.

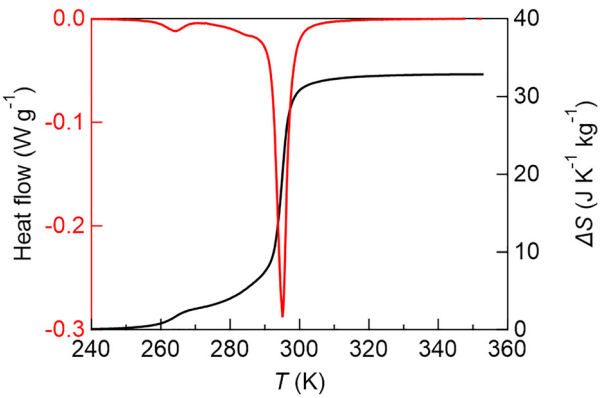

Fig. 2 DSC curve (red) of $YBaCo_2O_{5.5}$ measured during heating. Corresponding entropy change ΔS (black) calculated from the eqn (1) is also plotted (right axis). The entropy values refer to the value at 240 K.

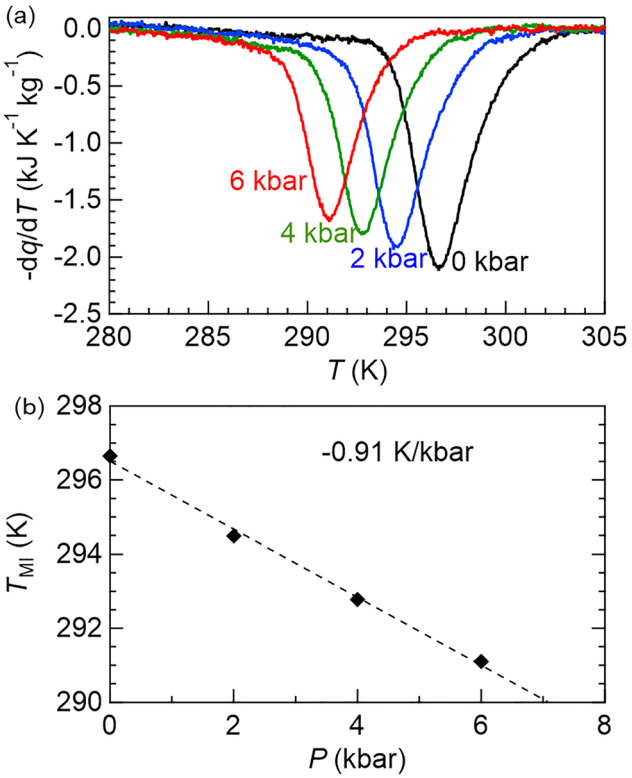

Fig. 3 (a) Heat flow curves divided by heating rate during heating in $YBaCo_2O_{5.5}$ under several pressures. (b) Pressure dependence of the DTA peak temperature. The dashed line corresponds to the linear fitting of the data.

To evaluate the cooling performance through the BCE, we calculated the temperature dependence of entropy S near T_{MI} under several pressures from the DTA data (Fig. 4a). The entropy S can be expressed as

$$S(T,P) = \int_{T_w}^{T} \frac{dq/dT}{T} dT + S_w(T_w,P), \quad (3)$$

where $S_w(T_w, P)$ is the entropy at the reference state with temperature T_w and pressure P. It is noted that S_w definitely depends on the pressure. However, we can still align the same baseline in the low-temperature-insulator phase despite the presence of a small isothermal entropy difference $\Delta S_w(P)$. $\Delta S_w(P)$ can be derived using Maxwell's relation:

$$\Delta S_w(P) = \int_0^P -(\partial V/\partial T)_H dH. \quad (4)$$

The maximum ΔS_w is 2.65 J K^{-1} kg^{-1} under 6 kbar, which is 8.9% of the entropy change at T_{MI} and at 0 kbar and is negligible in the current case. As shown in the S–T curves under several pressures, the observed entropy jump near T_{MI} decreases slightly with increasing pressure, which can be explained by the Clausius–Clapeyron equation as follows. While dT/dP is constant regardless of P, ΔV generally decreases with increasing P, thereby leading to a decrease in ΔS.

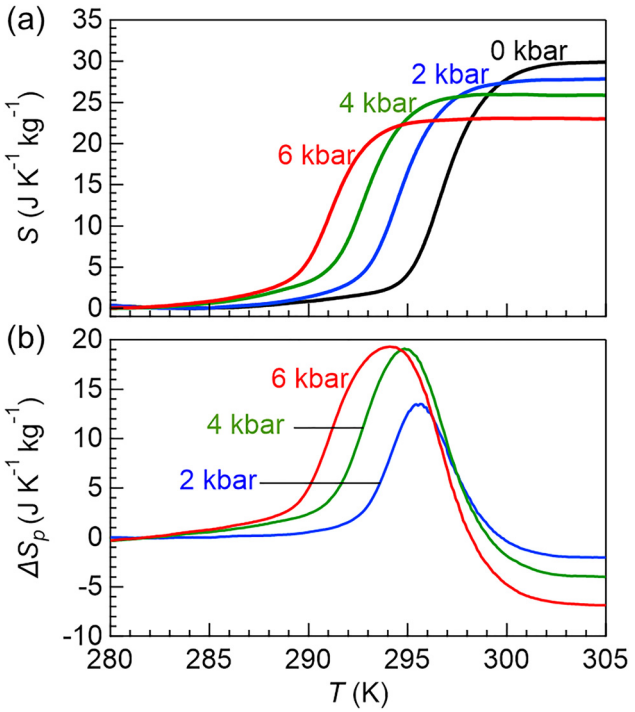

Fig. 4 (a) Temperature dependence of entropy S during heating process. Entropy S is calculated using the eqn (3). (b) Isothermal entropy changes ΔS_P of $YBaCo_2O_{5.5}$.

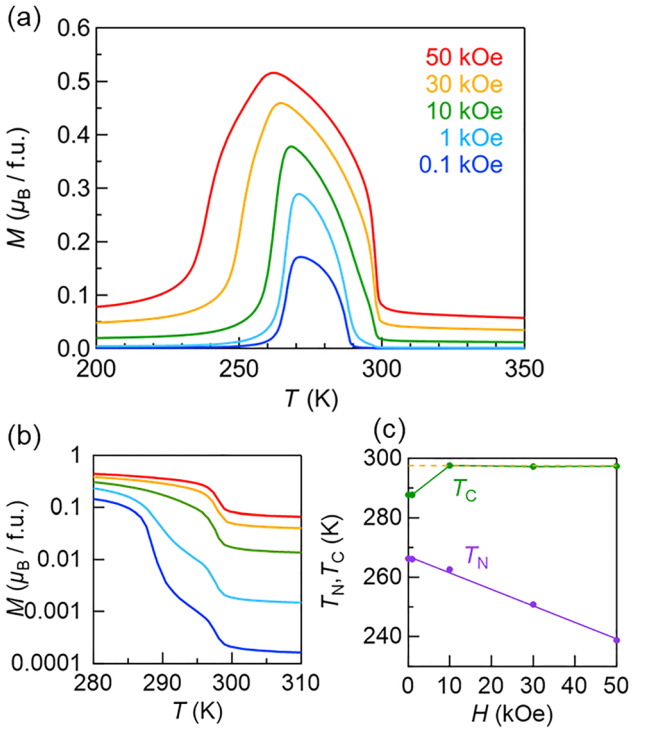

Fig. 5 (a) Temperature dependence of magnetization under several magnetic fields. (b) An enlarged view of the temperature dependence of magnetization near T_{MI} and T_C. (c) Magnetic field dependence of T_C and T_N. The yellow dotted line indicates T_{MI}.

The corresponding isothermal entropy change, ΔS_P $(T) = S$ $(P, T) - S$ $(0, T)$, is shown in Fig. 4(b). The maximum ΔS_P is 13.5 J K^{-1} kg^{-1} under 2 kbar, 19.1 J K^{-1} kg^{-1} under 4 kbar, and 19.3 J K^{-1} kg^{-1} under 6 kbar [Fig. 4(b)]. One might wonder why the maximum ΔS_P is almost the same under 4 and 6 kbar, because the overlap of the DTA peaks under 4 and 0 kbar is clearly larger than that under 6 and 0 kbar. As mentioned before, the observed entropy change near T_{MI} slightly decreases with increasing P. As a result, the maximum ΔS_P seems to saturate under approximately 4–6 kbar. The results demonstrate that approximately 2/3 of the entropy changes observed in the DSC measurement are utilized through the BCE under P = 4–6 kbar. In addition, the corresponding maximum adiabatic temperature change $\Delta T = T(S, 0) - T(S, P)$ is calculated to be 3.8 K under 4 kbar and 5.3 K under 6 kbar, producing the following refrigerant capacity (approximately expressed as the product of ΔS and ΔT.), 72.6 J kg^{-1} under 4 kbar and 102.3 J kg^{-1} under 6 kbar.[24]

Since $YBaCo_2O_{5.5}$ shows magnetic transitions, it is expected that some of the phase transitions can also be controlled by applying a magnetic field. Fig. 5(a) shows the temperature dependence of the magnetization under several magnetic fields. With decreasing temperature, the magnetization shows an increase at 297 K ($\sim T_{MI}$) under 0.1 kOe due to a change in the Co^{3+}-spin state, and the spin-state anomaly temperature does not change with increasing magnetic field (Fig. 5b). This means that the large latent heat near T_{MI} cannot be utilized through an MCE. On the other hand, ferrimagnetic ordering is formed between T_C and T_N, which could enable us to control the two magnetic transitions with a magnetic field. Under 0.1 kOe, a PM-FiM transition at T_C = 288 K and a FiM-AFM transition at T_N = 266 K are observed. In contrast to the anomaly at T_{MI}, T_C and T_N largely depend on H. The H dependence of T_C shows an unusual behavior. While the PM-FiM transition temperature T_C increases by increasing H up to 10 kOe, T_C does not change above H = 10 kOe (Fig. 5b and c). Accordingly, T_C appears to coincide with T_{MI}, suggesting that the second-order PM-FiM transition merges with the first-order MI transition and is observed as a single first-order phase transition. Here, it should be noted again that T_{MI} is independent of H, as confirmed in the electrical resistivity data under 0 and 5 T (Fig. S3). Thus, T_C is constant above H = 10 kOe, and a first-order-like discontinuous increase of the magnetization is especially observed under H = 50 kOe (Fig. 5a). On the other hand, the FiM-AFM transition temperature T_N linearly decreases with increasing H (Fig. 5a and c). The decrease in T_N under H is also confirmed by the resistivity data, as the jump in electrical resistivity at 266 K is suppressed under 50 kOe (Fig. S3). Summarizing the response of the phase transitions to H, T_C (T_N) tends to increase (decrease) with increasing H due to the stabilization of the ferrimagnetic phase, and only T_C saturates above 10 kOe due to the coincidence of T_C and T_{MI}.

To evaluate the cooling performance through the MCE, we evaluated the magnetic entropy change, ΔS_M, from the isothermal magnetization as a function of applied magnetic field. From the Maxwell relation,

$$(\partial S_M/\partial H)_T = \mu_0(\partial M/\partial T)_H, \quad (5)$$

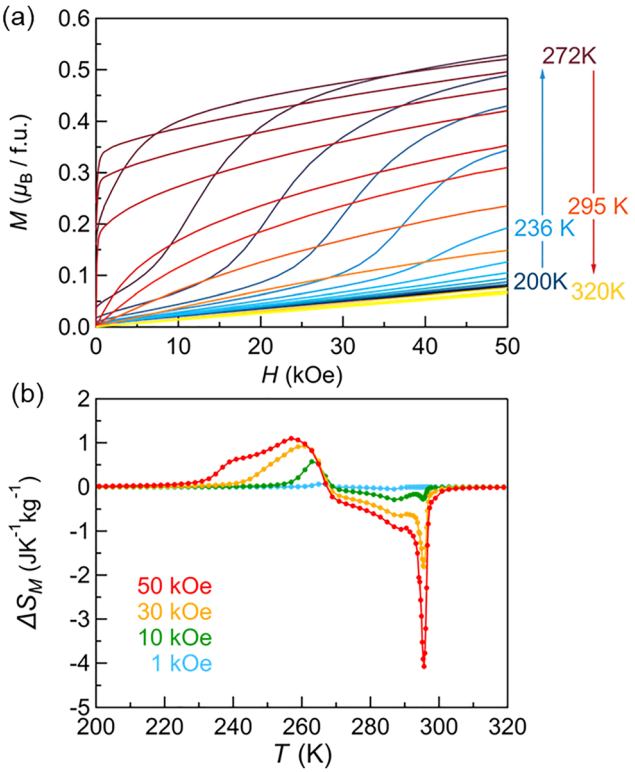

Fig. 6 (a) Isothermal magnetization between 200 and 320 K. (b) Temperature dependence of magnetic entropy change.

the magnetic entropy is described as

$$\Delta S_M = \mu_0 \int_0^H (\partial M/\partial T)_H dH, \quad (6)$$

By using the isothermal magnetization data from 200 to 320 K shown in Fig. 6(a), the magnetic entropy change ΔS_M is thus estimated by the following formula;

$$\Delta S_M[(2T + \Delta T)/2] = \mu_0 \int_0^H [M(T + \Delta T) - M(T)]/\Delta T dH, \quad (7)$$

where ΔT is the temperature internal at which the isothermal magnetization curves are measured (from 0.25 to 2 K in the present experiments) (see Fig. 6a). The resultant ΔS_M as a function of temperature is displayed in Fig. 6b. The maximum magnetic entropy change ($|\Delta S_M|$) under H = 50 kOe reaches 4.1 J K^{-1} kg^{-1} near T_C (T_{MI}) and 1.1 J K^{-1} kg^{-1} near T_N. Because the spontaneous magnetization of this compound in the ferrimagnetic phase is at most 0.4μ_B per f.u., the obtained maximum $|\Delta S_M|$ is not so large. Even so, the maximum $|\Delta S_M|$ near T_C under magnetic fields larger than 10 kOe becomes significant, reflecting the fact that the PM-FiM transition becomes of first order with the fixed T_C (=T_{MI}). Another characteristic of the MCE in $YBaCo_2O_{5.5}$ is that while ΔS_M near T_C is negative, that near T_N is positive. The result implies that in addition to the normal MCE near T_C, inverse MCE near T_N can be utilized in the single compound.

As presented above, the MI transition is sensitive to changes in pressure, thus showing the BCE. Considering that T_C coincides with T_{MI} above H = 10 kOe, applying pressure can also be expected to control the PM-FiM magnetic transition. We then performed magnetization measurements under several pressures. When H is small, like 0.1 kOe, T_{MI} shifts to lower temperatures, while T_C remains almost unchanged with increasing pressure (Fig. 7a, b and e). In contrast, when H is larger than 10 kOe, T_C (= T_{MI}) decreases with increasing pressure (Fig. 7c–e). We can therefore conclude that the PM-FiM transition can be tuned by applying pressure above H = 10 kOe, as well as the simultaneous metal–insulator transition.

We also mention the pressure dependence of the FiM-AFM transition temperature T_N, which is more complicated. When H is small like 0.1 kOe, T_N decreases monotonically with increasing pressure (Fig. 7a, b and e). Above H = 30 kOe, the trend is reversed, and T_N increases monotonically with increasing pressure. In particular, when H is 70 kOe, T_N shifts to higher temperatures by approximately 20 K under P = 8 kbar (Fig. 7e). These results suggest that the stability of the ferrimagnetic and antiferromagnetic phases is very sensitive to external pressure although their magnetic structures are still under debate.[18,25] While the decrease in T_N with increasing P

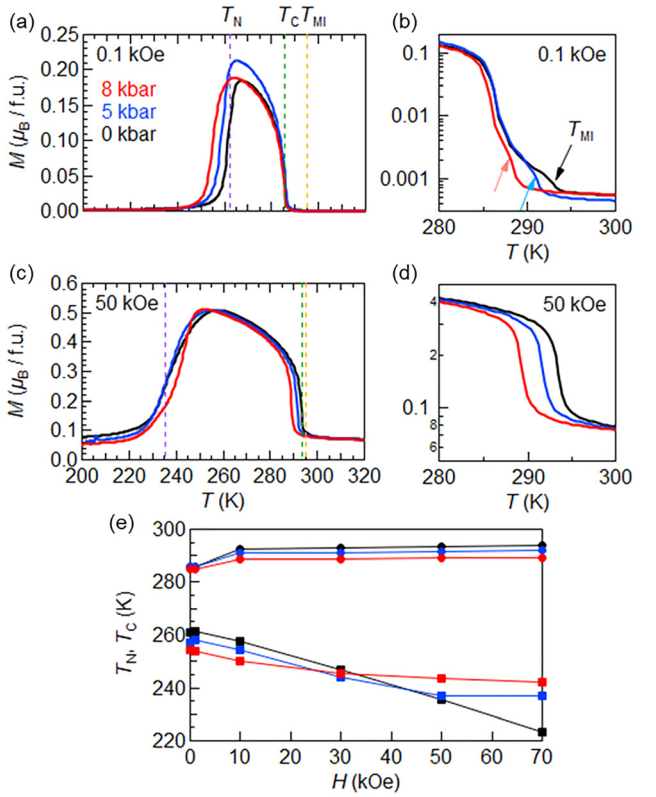

Fig. 7 (a) Temperature dependence of magnetization under several pressures while applying 0.1 kOe. (b) An enlarged view of the temperature dependence under 0.1 kOe near T_{MI} and T_C. (c) Temperature dependence of magnetization under several pressures while applying 50 kOe. (d) An enlarged view of the temperature dependence under 50 kOe near T_{MI} and T_C. (e) Magnetic field dependence of T_C and T_N under several pressures.

under low magnetic fields remains elusive, its increase under high magnetic fields (≧30 kOe) can be interpreted through the coincidence of T_s and T_N. Based on the Clausius–Clapeyron relation, the negligible latent heat and moderately large positive ΔV at T_s imply a large dT_s/dP, leading to a significant upward shift of T_s under P. Considering that T_N is suppressed by magnetic fields, T_s and T_N. are expected to coincide under high pressures and fields. If we assume a constraint where T_s cannot surpass T_N (analogous to the relationship $T_C \leqq T_{MI}$), it is natural that T_N increases with increasing P under high magnetic fields, following the shift of T_s.

Finally, we consider the effect of the coincidence of T_C and T_{MI} above H = 10 kOe on the thermal properties. Without a magnetic field, the entropy changes due to the Co^{3+}-spin-state change, the MI transition, and the structural change should contribute to the large latent heat (8.8 J g^{-1}) near T_{MI} in $YBaCo_2O_{5.5}$. Above H = 10 kOe, the first-order PM-FiM magnetic transition is also induced at T_{MI}, implying that the magnetic entropy change of Co^{3+} magnetic moments by magnetic ordering also contributes to the latent heat. Consequently, the enhanced latent heat could improve the BCE under high magnetic fields. As such, this material not only exhibits both barocaloric and magnetocaloric effects but also has the potential to exhibit more efficient caloric effects by combining multiple external fields. Therefore, a future challenge is to investigate the thermal properties under simultaneous application of pressure and magnetic fields.

Conclusions

We have found that the A-site layer-ordered double perovskite oxide $YBaCo_2O_{5.5}$ shows multiple caloric effects driven by the successive phase transitions at T_{MI}, T_C, and T_N. The Co^{3+}-spin state in $YBaCo_2O_{5.5}$ induces the first-order MI transition with a negative-thermal-expansion-like volume change near room temperature, which contributes to a large latent heat of 8.8 J g^{-1}. Most of the corresponding entropy change (∼19 J K^{-1} kg^{-1}) is utilized under 4–6 kbar *via* an inverse barocaloric effect. Applying magnetic fields can control PM-FiM and FiM-AFM transitions below T_{MI}, inducing normal and inverse magnetocaloric effects, respectively. Above 10 kOe, the PM-FiM transition merges with the metal–insulator transition as a single first-order transition. This not only increases the maximum $|\Delta S_M|$ near T_C (=T_{MI}) but also could enhance the latent heat originating in the discontinuous magnetic entropy change of Co^{3+} magnetic moments. In addition, the coincidence of T_C and T_{MI} under high magnetic fields enables us to control the PM-FiM transition and the simultaneous MI transition by applying pressure, potentially producing the more efficient inverse barocaloric effect. We believe that the present results will serve as a catalyst for further exploration of novel thermal properties by applying multiple external fields in transition-metal oxides.

Conflicts of interest

There are no conflicts to declare.

Data availability

The data that support the findings of this study are available upon request from the authors.

Supplementary information (SI): results of the Rietveld refinement of the synchrotron X-ray diffraction data at 300 and 250 K, structural parameters at 300 and 250 K, temperature dependence of the synchrotron X-ray diffraction data and the refined lattice parameters, and temperature dependence of electrical resistivity under 0 and 50 kOe for $YBaCo_2O_{5.5}$. See DOI: https://doi.org/10.1039/d6ma00234j.

Acknowledgements

We thank S. Kawaguchi and S. Kobayashi at SPring-8 for their assistance with the SXRD experiments, M. Iihoshi and R. Watanabe at Kyoto University for their assistance with the SXRD experiments, and K. Ji at Kyoto university and P. Woodward at the Ohio State University for fruitful discussions. The synchrotron radiation experiments were performed at the Japan Synchrotron Radiation Research Institute, Japan (proposal No. 2023B1593, 2024A1727, and 2025A2025). This work was partly supported by Grants-in-Aid for Scientific Research (No. 20H00397, 23H05457, and 23K13814) and by a grant to the Integrated Research Consortium on Chemical Sciences from the Ministry of Education, Culture, Sports, Science and Technology (MEXT) of Japan. This work was also supported by the Japan Science and Technology Agency (JST) as part of the Adopting Sustainable Partnerships for Innovative Research Ecosystem (ASPIRE) program, Grant Number JPMJAP2314, and by research grants for Nippon Sheet Glass Foundation for Materials Science and Engineering, Toyota Physical and Chemical Research Institute, and Tokuyama Science Foundation.

References

1 A. Fallahi, G. Guldentops, M. Tao, S. Granados-focil and S. Van Dessel, Review on solid-solid phase change materials for thermal energy storage: molecular structure and thermal properties, *Appl. Therm. Eng.*, 2017, **127**, 1427–1441.
2 J. Liu, T. Gottschall, P. K. Skokov, D. J. Moore and O. Gutfleisch, Giant magnetocaloric effect driven by structural transitions, *Nat. Mater.*, 2012, **11**, 620–626.
3 V. K. Pecharsky and K. A. Gschneidner Jr, Magnetocaloric effect and magnetic refrigeration, *J. Magn. Magn. Mater.*, 1999, **200**, 44–56.
4 D. Matsunami, A. Fujita, K. Takenaka and M. Kano, Giant barocaloric effect enhanced by the frustration of the antiferromagnetic phase in Mn_3GaN, *Nat. Mater.*, 2015, **14**, 73–78.
5 L. Mañosa, *et al.*, Giant solid-state barocaloric effect in the Ni–Mn–In magnetic shape-memory alloy, *Nat. Mater.*, 2010, **9**, 478–481.
6 A. S. Mischenko, Q. Zhang, J. F. Scott, R. W. Whatmore and N. D. Mathur, Giant Electrocaloric Effect in Thin-Film $PbZr_{0.95}Ti_{0.05}O_3$, *Science*, 2006, **311**, 1270–1271.

7 B. Neese, *et al.*, Large Electrocaloric Effect in Ferroelectric Polymers Near Room Temperature, *Science*, 2008, **321**, 821–823.
8 S. Ohkoshi, *et al.*, Giant adiabatic temperature change and its direct measurement of a barocaloric effect in a charge-transfer solid, *Nat. Commun.*, 2023, **14**, 8466.
9 X. Tang, *et al.*, Magnetic refrigeration material operating at a full temperature range required for hydrogen liquefaction, *Nat. Commun.*, 2022, **13**, 1817.
10 V. K. Pecharsky and K. A. Gschneidner, Giant Magnetocaloric Effect in $Gd_5(Si_2Gi_2)$, *Phys. Rev. Lett.*, 1997, **23**, 4494–4497.
11 H. Wada and Y. Tanabe, Giant magnetocaloric effect of $MnAs_{1-x}Sb_x$, *Appl. Phys. Lett.*, 2001, **79**, 3302–3304.
12 A. Aznar, *et al.*, Giant barocaloric effects over a wide temperature range in superionic conductor AgI, *Nat. Commun.*, 2017, **8**, 1851.
13 K. Fukamichi, A. Fujita and S. Fujieda, Large magnetocaloric effects and thermal transport properties of $La(FeSi)_{13}$ and their hydrides, *J. Alloys Compd.*, 2006, **408–412**, 307–312.
14 P. M. Woodward and P. Karen, Mixed Valence in $YBaFe_2O_5$, *Inorg. Chem.*, 2003, **42**, 1121–1129.
15 D. Matsunami and A. Fujita, Electrocaloric effect of metal–insulator transition in VO_2, *Appl. Phys. Lett.*, 2015, **106**, 042901.
16 Y. Kosugi, *et al.*, Colossal Barocaloric Effect by Large Latent Heat Produced by First-Order Intersite-Charge-Transfer Transition, *Adv. Funct. Mater.*, 2021, **31**, 1–7.
17 D. Akahoshi and Y. Ueda, Oxygen Nonstoichiometry, Structures, and Physical Properties of $YBaCo_2O_{5+x}$ ($0.00 \leq x \leq 0.52$), *J. Solid State Chem.*, 2001, **156**, 355–363.
18 D. D. Khalyavin, D. N. Argyriou, U. Amann, A. A. Yaremchenko and V. V. Kharton, Spin-state ordering and magnetic structures in the cobaltites $YBaCo_2O_{5+\delta}$ (δ = 0.50 and 0.44), *Phys. Rev. B: Condens. Matter Mater. Phys.*, 2007, **75**, 134407.
19 H. M. Rietveld, A profile refinement method for nuclear and magnetic structures, *J. Appl. Crystallogr.*, 1969, **2**, 65–71.
20 F. Izumi and K. Momma, Three-Dimensional Visualization in Powder Diffraction, *Solid State Phenom.*, 2007, **130**, 15–20.
21 K. Momma and F. Izumi, VESTA 3 for three-dimensional visualization of crystal, volumetric and morphology data, *J. Appl. Crystallogr.*, 2011, **44**, 1272–1276.
22 P. J. Pantoja, C. Frontera, J. H. Martin, J. Herrero, L. Munoz and J. Garcia, Spin state and structural changes at the metal–insulator transition in $YBaCo_2O_{5.5}$ by synchrotron X-rays, *J. Appl. Phys.*, 2012, **111**, 07D710.
23 Y. Kosugi, *et al.*, Giant multiple caloric effects in charge transition ferrimagnet, *Sci. Rep.*, 2021, **11**, 12682.
24 M. E. Wood and W. H. Potter, General analysis of magnetic refrigeration and its optimization using a new concept: maximization of refrigerant capacity, *Cryogenics*, 1985, **25**, 667.
25 R. Article, D. P. Kozlenko, N. O. Golosova and B. N. Savenko, Magnetic ground state and the spin-state transitions in $YBaCo_2O_{5.5}$, *Eur. Phys. J. B*, 2009, **70**, 327–334.